Japanese Journal of Radiology (2022) 40:38–47
https://doi.org/10.1007/s11604-021-01184-8

ORIGINAL ARTICLE

A novel strategy to develop deep learning for image super-resolution using original ultra-high-resolution computed tomography images of lung as training dataset

Hitoshi Kitahara[1] · Yukihiro Nagatani[1] · Hideji Otani[1] · Ryohei Nakayama[2] · Yukako Kida[1] · Akinaga Sonoda[1] · Yoshiyuki Watanabe[1]

Received: 24 May 2021 / Accepted: 21 July 2021 / Published online: 28 July 2021

Abstract

Purpose To improve the image quality of inflated fixed cadaveric human lungs by utilizing ultra-high-resolution computed tomography (U-HRCT) as a training dataset for super-resolution processing using deep learning (SR-DL).

Materials and methods Image data of nine cadaveric human lungs were acquired using U-HRCT. Three different matrix images of U-HRCT images were obtained with two acquisition modes: normal mode (512-matrix image) and super-high-resolution mode (1024- and 2048-matrix image). SR-DL used 512- and 1024-matrix images as training data for deep learning. The virtual 2048-matrix images were acquired by applying SR-DL to the 1024-matrix images. Three independent observers scored normal anatomical structures and abnormal computed tomography (CT) findings of both types of 2048-matrix images on a 3-point scale compared to 1024-matrix images. The image noise values were quantitatively calculated. Moreover, the edge rise distance (ERD) and edge rise slope (ERS) were also calculated using the CT attenuation profile to evaluate margin sharpness.

Results The virtual 2048-matrix images significantly improved visualization of normal anatomical structures and abnormal CT findings, except for consolidation and nodules, compared with the conventional 2048-matrix images ($p < 0.01$). Quantitative noise values were significantly lower in the virtual 2048-matrix images than in the conventional 2048-matrix images ($p < 0.001$). ERD was significantly shorter in the virtual 2048-matrix images than in the conventional 2048-matrix images ($p < 0.01$). ERS was significantly higher in the virtual 2048-matrix images than in the conventional 2048-matrix images ($p < 0.01$).

Conclusion SR-DL using original U-HRCT images as a training dataset might be a promising tool for image enhancement in terms of margin sharpness and image noise reduction. By applying trained SR-DL to U-HRCT SHR mode images, virtual ultra-high-resolution images were obtained which surpassed the image quality of unmodified SHR mode images.

Keywords Deep learning · Artificial intelligence · Convolutional neural networks · Cadaveric lung · Ultra-high-resolution computed tomography

Introduction

The usage of artificial intelligence (AI) in diagnostic imaging is undergoing extensive evaluation and application in clinical settings. Higaki et al. described techniques that improve medical image quality using a convolutional neural networks (CNN)-based algorithm as follows: (1) noise and artifact reduction, (2) super-resolution, and (3) image acquisition and reconstruction [1]. Noise and artifact reduction lead to reduced radiation exposure and decreased imaging time, and super-resolution leads to the improvement of diagnostic ability. Dong et al. reported the

✉ Hitoshi Kitahara
hitoshik@belle.shiga-med.ac.jp

[1] Department of Radiology, Shiga University of Medical Science, Seta Tsukinowa-Cho, Otsu, Shiga 520-2192, Japan

[2] Department of Electronic and Computer Engineering, Ritsumeikan University, 1-1-1 Noji-higashi, Kusatsu, Shiga 525-8577, Japan

effectiveness of a CNN-based algorithm for reconstruction of high-resolution images from low-resolution ones [2]. In addition, Umehara et al. successfully restored original images using a CNN-based algorithm from intentionally downsampled low-resolution chest computed tomography (CT) images [3].

While these preceding studies show promising results of CNN-based super-resolution methods, the strategy has limitations. In commonly used CT devices, the maximum matrix size is 512 and the maximum spatial resolution is limited to around 0.3 mm regardless of the field-of-view (FOV). Therefore, 512-matrix CT images are artificially degraded and used as training data alongside the original 512-matrix images as a training dataset for the AI algorithm to restore the degraded images. Thus, limitations of matrix size and spatial resolution of training images have been a bottleneck of developing CNN-based super-resolution algorithms for CT.

There has been little progress in increasing in-plane spatial resolution over the last 30 years until ultra-high-resolution CT (U-HRCT) became available for clinical settings. In U-HRCT, introduced in 2017, the minimum focus size of the X-ray tube is 0.4 × 0.5 mm, the detector element size is 0.25 × 0.25 mm, and a spatial resolution of 0.14 mm was achieved in a metal slit phantom experiment [4]. A study by Yanagawa et al. using inflated fixed cadaveric human lungs concluded that U-HRCT produced images of significantly superior quality to 320-detector-row CT systems with area detectors [5]. In clinical research, Iwasawa et al. recently reported the usefulness of U-HRCT in the diagnosis of novel coronavirus (COVID-19) pneumonia [6].

The U-HRCT scanner has three scan modes: normal resolution (NR), high-resolution (HR), and super-high-resolution (SHR). The quality of NR images is expected to be equivalent to the conventional 512-matrix image. On the other hand, the maximum matrix size in SHR mode is 2048, the maximum spatial resolution is 0.14 mm, and the image quality is better than common 512-matrix images as reported by Hata and Yanagawa [4, 5]. By utilizing different image acquisition modes of U-HRCT, we can obtain actual CT images of different resolutions at the same slice position, which enables us to use actual CT images of different resolution as a training dataset for a deep learning-based super-resolution algorithm. Therefore, we developed a CNN-based super-resolution algorithm using 512-matrix images from the NR mode and 1024-matrix images from the SHR mode obtained from inflated fixed cadaveric human lungs as a training dataset. We then applied the trained CNN-based algorithm to 1024-matrix images from the SHR mode and reconstructed virtual 2048-matrix images, and then compared them to conventional 2048-matrix images from the SHR mode to examine the degree of improvement of image quality.

The purpose of this study is to develop a CNN-based super-resolution algorithm using actual U-HRCT images as a training dataset, and to reconstruct CT images of inflated fixed cadaveric human lungs which surpass the original U-HRCT image in image quality.

Materials and methods

Our institutional review board approved this experimental study and waived the requirement for obtaining informed patient consent (No. R2020-178).

U-HRCT scanner

A U-HRCT scanner (Aquilion Precision; Canon Medical Systems, Tochigi, Japan) was used in this study. The detector element size was 0.25 × 0.25 mm; the detector had 1792 channels with 160 rows. The minimum focus size of the X-ray tube was 0.4 × 0.5 mm. The U-HRCT scanner has three scan modes: NR, HR, and SHR. The NR mode is similar to standard CT, in which 896 detector channels with 0.5 × 0.5 mm size are used and only a 512 × 512 matrix and a 0.5 mm slice thickness are available. In the SHR mode, 1792 detector channels with 0.25 × 0.25 mm size are used, and 512 × 512, 1024 × 1024, and 2048 × 2048 matrix sizes with a 0.25 mm slice thickness are available, thereby providing high-resolution images in both the in-plane and body-axis directions.

Cadaveric human lungs

Nine cadaveric human lungs were inflated and fixed using the Heitzman method [7]. The lungs were distended through the main bronchus with fixative fluid containing polyethylene glycol 400, 95% ethyl alcohol, 40% formalin, and water at a ratio of 10:5:2:3. The specimens were immersed in fixative fluid for 2 days and then air-dried.

The pathological diagnoses of these nine lungs were as follows: pulmonary lymphangitic carcinomatosis ($n = 1$), lung cancer ($n = 2$), metastasis from colon cancer ($n = 1$), metastases from gastric cancer ($n = 1$), multiple myeloma ($n = 1$), pneumocystis pneumonia ($n = 1$), rheumatoid arthritis-interstitial pneumonia ($n = 1$), and early-stage idiopathic pulmonary fibrosis ($n = 1$).

U-HRCT image acquisition

Image data of the nine inflated fixed cadaveric human lungs were acquired with the U-HRCT scanner. The U-HRCT images were obtained with a 0.5 s gantry rotation, 200 mm FOV, 120 kVp, and two types of acquisition modes: NR mode (helical scan) [280 mA, 896 channels per row,

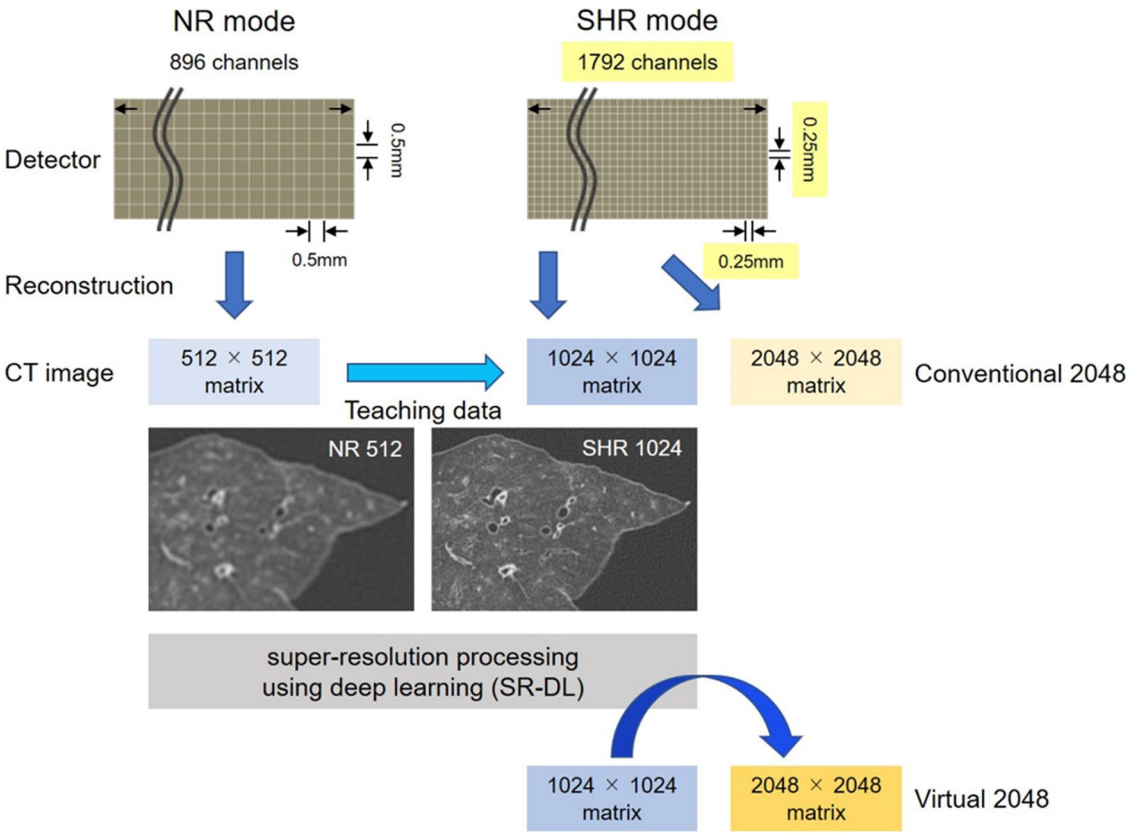

Fig. 1 The raw data were acquired in the U-HRCT NR mode (detector 0.5×0.5 mm), and the 512×512 matrix images were then reconstructed. Raw data were also acquired in U-HRCT SHR mode (detector 0.25×0.25 mm), and the 1024×1024 matrix images and 2048×2048 matrix images (Conventional 2048) were then reconstructed. The SR-DL was trained using the 512×512 matrix images as low-resolution data and the 1024×1024 matrix images as high-resolution data. Then, the 1024×1024 matrix images were applied to this trained SR-DL to construct the 2048×2048 matrix images (Virtual 2048). *U-HRCT* ultra-high-resolution computed tomography, *NR* normal resolution, *SHR* super-high resolution, *SR-DL* super-resolution processing using deep learning

0.5 mm×80 rows, pitch factor (PF): 0.638, volumetric CT dose index (CTDIvol): 14.2 mGy] and SHR mode (helical scan) [260 mA, 1792 channels per row, 0.25 mm×160 rows, PF: 0.569, CTDIvol: 14.3 mGy]. The NR mode helical scan was reconstructed with a 512×512 matrix size and the SHR mode helical scan was reconstructed with both 1024×1024 and 2048×2048 matrix sizes. In this study, we refer to the conventional 1024×1024 matrix size image as "c1024-images," and the conventional 2048×2048 matrix size image as "c2048-images." These images had the same cross-sectional levels because all image data were acquired at the same time. All U-HRCT images of 0.5-mm thickness were reconstructed using a lung kernel (FC51) and adaptive iterative dose reduction in three dimensions (AIDR 3D). Although it was possible to obtain 0.25 mm-thick images in the SHR mode, we set the slice thickness to 0.5 mm to match the slice thickness of the NR mode. This is to obtain training dataset of the same slice thickness. All CT series were anonymized and transferred to a distant workstation viewer by one chest radiologist who was not involved in image evaluation.

Super-resolution processing using deep learning

The super-resolution processing using deep learning (SR-DL) proposed in this study was based on a very deep super-resolution neural networks [8]. The SR-DL estimates high-frequency components in a high-resolution CT image from a low-resolution CT image. The high-resolution CT image is then generated by adding the estimated high-frequency components to the low-resolution image. The SR-DL consists of an input layer, 13 repeated applications of a convolutional layer and a rectified linear unit (ReLU), and a regression layer (output layer). Each convolutional layer contained 64 filters with a kernel size of 3×3.

In this study, the training dataset images and the test dataset images were not obtained from the same lungs. We developed two methods for super-resolution, named SR-DL1

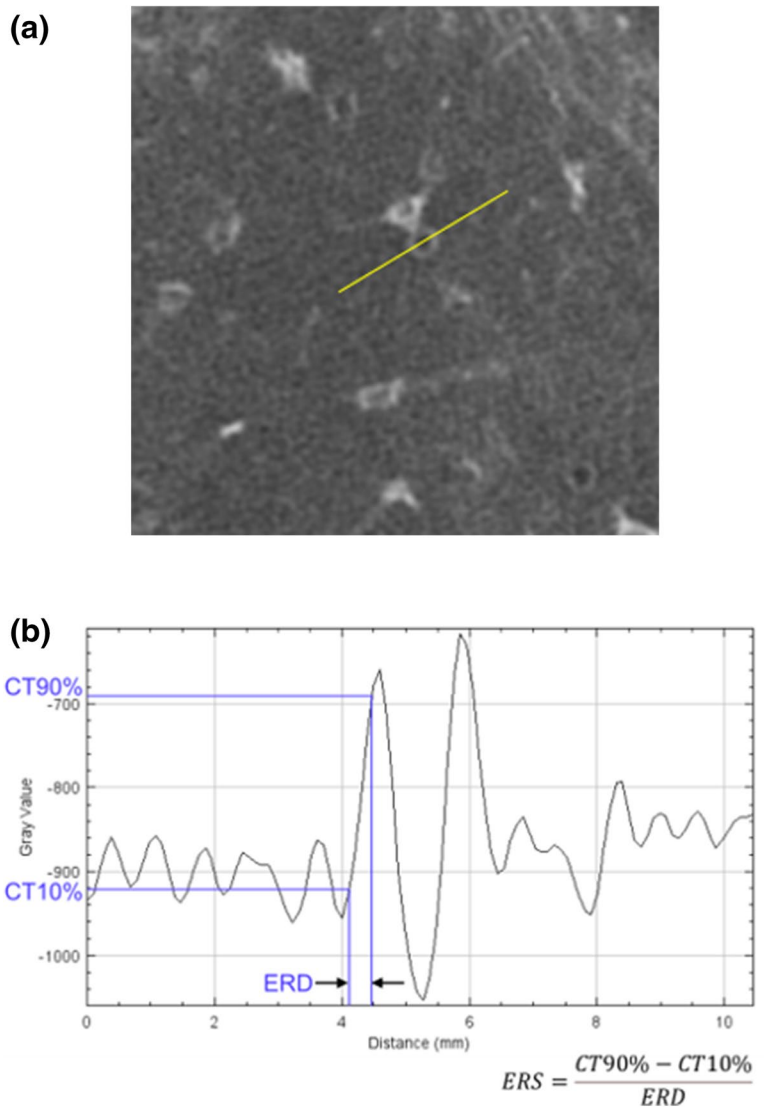

Fig. 2 **a** A straight line that traverses the bronchiolar wall almost vertically. **b** The CT attenuation profile along the straight line shown in (**a**). *CT* computed tomography

and 2. Nine patients' data were randomly divided into two datasets (four patients' data; group A, and five patients' data; group B). SR-DL1 was developed by utilizing group A as training dataset and evaluated by utilizing group B as test dataset. SR-DL2 was developed vice versa. The low-resolution CT image up-sampled using bicubic interpolation to match the size of the high-resolution CT image was inputted to the input layer of the SR-DL. In the training of the SR-DL, the residual images, which were the "difference" images between the input low-resolution CT images and the corresponding high-resolution CT images, were used as the desired output values (teaching signals) in the output layer of the SR-DL. The parameters in the SR-DL were updated such that the mean squared errors between the output of the proposed SR-DL and the corresponding teacher signals were minimized. To test the SR-DL, an up-sampled low-resolution CT image in the test dataset was input to the trained SR-DL. The high-resolution CT image was then generated by adding the estimated high-frequency components to the input low-resolution image (Fig. 1).

Virtual 2048-matrix image acquisition by SR-DL

The trained SR-DL was applied to the c1024-images to obtain virtual 2048-matrix images (v2048-images), as shown in Fig. 1. First, a c1024-image is up-sampled to a 2048-matrix image by bicubic interpolation. It is then input to the trained SR-DL, where the high-frequency components are estimated. Finally, by adding it to the input image, a v2048-image was generated. All images were anonymized and transferred to a distant workstation viewer by a chest radiologist with 21 years of experience.

Table 1 Subjective image evaluation

CT finding	GGO*	B/B*	Emp*	Nodule	IST*	Consolidation	Ret*	Nor*
N	66	22	18	15	10	12	28	40
Conventional 2048-matrix image	2.00 ± 0.00	2.00 ± 0.00	2.00 ± 0.00	2.00 ± 0.00	2.00 ± 0.00	2.00 ± 0.00	2.00 ± 0.00	2.00 ± 0.00
Virtual 2048-matrix image	2.97 ± 0.17	2.86 ± 0.35	3.00 ± 0.00	2.27 ± 0.70	2.90 ± 0.32	2.17 ± 0.39	2.89 ± 0.31	3.00 ± 0.00
p value	1.28×10^{-15}	1.45×10^{-5}	2.47×10^{-5}	0.182	0.00335	0.346	6.21×10^{-7}	2.67×10^{-10}

Data are presented as mean ± SD. Data of the subjective image evaluation were statistically analyzed using the Wilcoxon signed-rank test

GGO ground-glass opacity, *B/B* bronchiectasis with bronchial wall thickening, *Emp* emphysematous change, *IST* interlobular septal thickening, *Ret* reticular opacity, *Nor* normal anatomical structure

*There was a significant difference between c2048-images and v2048-images ($p < 0.05$)

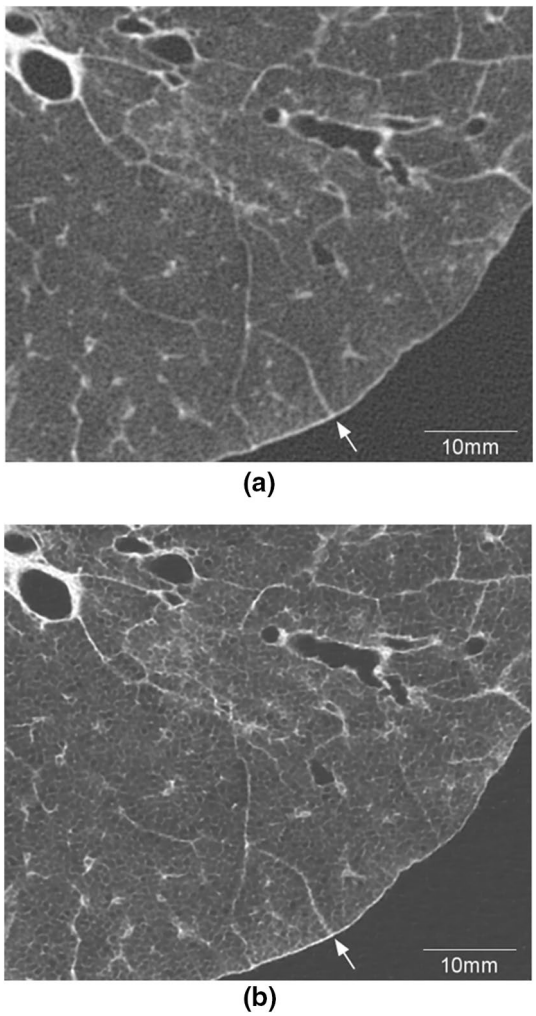

Fig. 3 **a** The conventional 2048-matrix image and **b** the virtual 2048-matrix image. The interlobular septal thickening (white arrow) is more clearly seen in (**b**) than in (**a**)

Subjective image evaluation

One chest radiologist, who was not involved in image evaluation, recorded information on the normal anatomical structures (vessels and bronchi) and abnormal CT findings in each inflated fixed cadaveric human lung. Abnormal CT findings include ground-glass opacity (GGO), bronchiectasis with bronchial wall thickening, emphysematous change, nodules, interlobular septal thickening, consolidation, and reticular opacity. There were 211 findings from 56 slices, which consisted of 66 GGOs, 22 bronchiectasis with bronchial wall thickening, 18 emphysematous changes, 15 nodules, 10 interlobular septal thickening, 12 consolidation, 28 reticular opacity, and 40 normal anatomical structures. Three independent radiologists read all 56 images and evaluated them on an 8.8-megapixel, 31.1-inch color LCD (4 K resolution) monitor without prior knowledge of histopathological diagnoses or image acquisition parameters. These images were displayed with a window level of -600 Hounsfield units (HU) and a window width of 1600 HU. The image display could be up to double the magnification as needed. When enlarging the image, the enlargement ratios of the c1024-image and the 2048-matrix image had to be the same. The chest radiologist created an evaluation map in which the evaluation target regions in the c1024-images were marked with a collar marker so that the evaluator could easily recognize the evaluation target regions. For each inflated fixed cadaveric human lung, the blinded 2048-matrix images, which were either the c2048-images or the v2048-images, and the reference c1024-images were evaluated side-by-side on the 8 M monitor. Because all images were reconstructed from common raw data, the slice positions were exactly the same. Abnormal CT findings and normal anatomical structure were subjectively graded using a 3-point scale:

Table 2 Margin sharpness

Inflated fixed cadaveric lung		1	2	3	4	5	6	7	8	9	Mean ± SD	*p* value
Anatomical structure		PV	PV	Brl	PV	PV	ILS	PA	Br	PV		
ERD (mm)	Conventional 2048-matrix image	0.335	0.29	0.383	0.413	0.387	0.329	0.312	0.263	0.335	0.34 ± 0.048	0.0039
	Virtual 2048-matrix image	0.223	0.205	0.313	0.317	0.327	0.224	0.226	0.182	0.244	0.25 ± 0.054	
ERS (HU/mm)	Conventional 2048-matrix image	1432.38	1199.88	571.52	1055.39	1246.9	665.899	1564.97	1193.54	919.596	1094.45 ± 329.58	0.0039
	Virtual 2048-matrix image	3072.69	2146.34	966.32	1636.7	1551.02	1082.63	2570.84	2407.55	2166.55	1955.63 ± 699.79	

Data for margin sharpness were statistically analyzed using the Wilcoxon signed-rank test

ERD edge rise distance, *ERS* edge rise slope, *Br* bronchus, *Brl* bronchiole, *ILS* interlobular septum, *PA* pulmonary artery, *PV* pulmonary vein

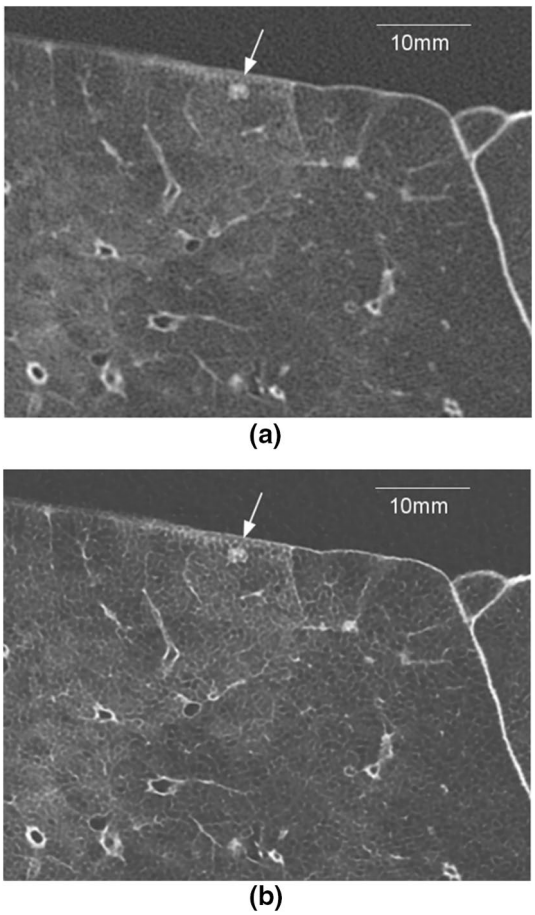

Fig. 4 **a** The conventional 2048-matrix image and **b** the virtual 2048-matrix image. The fine reticular opacity in the ground-glass opacity is more conspicuous in (**b**) than in (**a**). There is also a subpleural nodule (white arrow)

(1), poor image quality (i.e., it was possible to detect structures but difficult to clearly evaluate their margin or internal characteristics); (2), fair image quality (i.e., the margin or internal characteristics can be detected and evaluated as well as in the reference images); (3), excellent image quality (i.e., it was easy to detect findings and to evaluate their margin or internal characteristics without any indistinct findings).

Quantitative image noise evaluation

Quantitative image noise measurements were calculated by measuring the standard deviations (SDs) in circular regions of interest (ROIs) 20 mm in diameter using ImageJ software (National Institutes of Health, Bethesda, MD; http://rsb.info.nih.gov/ij). ROIs were placed in three homogeneous parts of air adjacent to every lung [9] and in exactly the same location on both the c2048-image and the

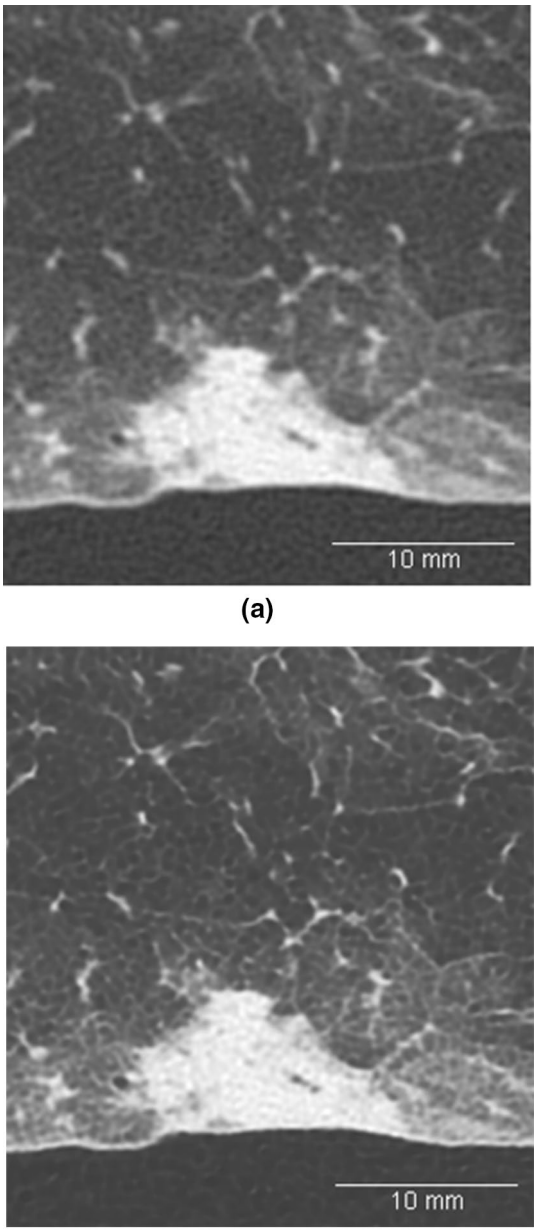

Fig. 5 **a** The conventional 2048-matrix image and **b** the virtual 2048-matrix image. The consolidation is drawn to the same extent in (**a**) and (**b**), but the edge of consolidation and air bronchogram are slightly more conspicuous in (**b**) than in (**a**)

v2048-image. The SDs from these ROIs were statistically compared between c2048-images and the v2048-images.

Margin sharpness

We selected blood vessels, bronchi, bronchioles, and the interlobular septum in the lung field that were clearly visible in the c2048-image and created a CT attenuation profile along a straight line that traversed them almost vertically using ImageJ software (National Institutes of Health) and its particle analysis tool (plot profile). The CT attenuation profiles were generated at precisely the same location for the c2048-image and v2048-image. We then measured the width of the edge response at the boundary of the blood vessel, bronchus, bronchiole, or interlobular septum determined by the 10–90% edge rise distance (ERD) (mm), and then calculated the edge rise slope (ERS) [ERS = (CT90% − CT10%)/ERD] (HU/mm) [10] (Fig. 2). The ERD and the ERS of the c2048-images and the v2048-images were statistically compared.

Statistical analysis

All statistical analyses were performed using the free software EZR [11]. The median values of the subjective scores of the three independent radiologists and the statistical significance of any differences between them from the c2048-images and the v2048-images were assessed using the Wilcoxon signed-rank test. The ERD and the ERS of the c2048-images and the v2048-images were compared using the Wilcoxon signed-rank test. Image noise in the c2048-images and the v2048-images was compared using the paired *t* test. Statistical significance was set at $p < 0.05$.

Results

Subjective image evaluation

The image quality scores for abnormal CT findings and the normal anatomical structures of the c2048-image and the v2048-image are summarized in Table 1. In v2048-images, GGO (the presence of a hazy increase in lung density on HRCT without obscuration of underlying vessels or the walls of airways) [12], bronchiectasis with bronchial wall thickening, emphysematous change, interlobular septal thickening, and reticular opacity were significantly more frequent than in c2048-images ($p < 0.01$) (Fig. 3). There were no significant differences in nodule and consolidation scores between images. Moreover, in the v2048-images, the normal anatomical structure scores were also significantly higher than those in the c2048-images ($p < 0.01$).

Quantitative image noise evaluation

Quantitative noise values were significantly lower in the v2048-image (11.28 ± 2.99) than in the c2048-image (28.76 ± 2.97) ($p < 0.001$).

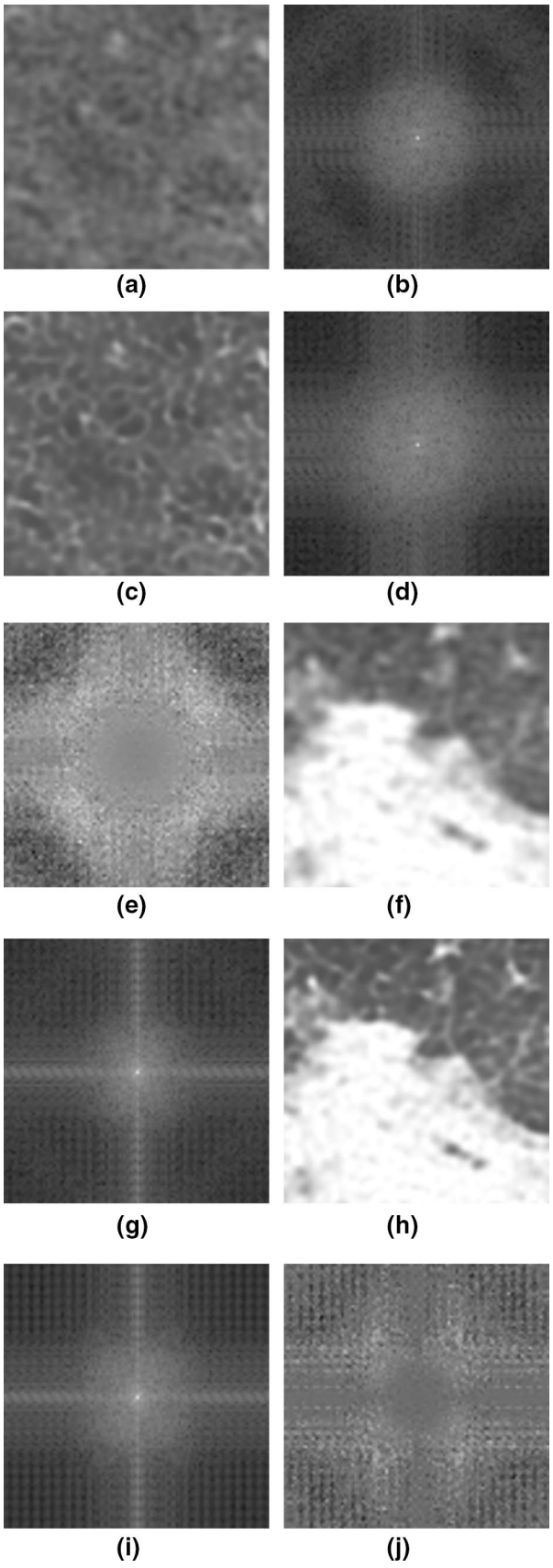

Fig. 6 **a** Conventional 2048-matrix image of GGO. **b** FFT power spectrum of (**a**). **c** Virtual 2048-matrix image of GGO. **d** FFT power spectrum of (**c**). **e** Subtraction image of (**d**–**b**). **f** Conventional 2048-matrix image of consolidation. **g** FFT power spectrum of (**f**). **h** Virtual 2048-matrix image of consolidation. **i** FFT power spectrum of (**h**). **j** Subtraction image of (**i**–**g**). *GGO* ground-glass opacity, *FFT* fast Fourier transform

Margin sharpness

As shown in Table 2, the ERD was significantly shorter in the v2048-images (0.25 ± 0.054 mm) than in the c2048-images (0.34 ± 0.048 mm) ($p < 0.01$); the ERS (mean ± SD) was significantly higher in the v2048-images (1955.63 ± 699.79 HU/mm) than in the c2048-images (1094.45 ± 329.58 HU/mm) ($p < 0.01$).

Discussion

We created a super-resolution algorithm by training SR-DL using U-HRCT NR and SHR mode images as a training dataset. Preceding super-resolution algorithms were trained to restore image quality that was intentionally deteriorated, but our algorithm has for the first time been trained to improve the image quality of original CT images. This was enabled by the introduction of U-HRCT to clinical settings, which could obtain CT images of different resolutions at the same slice position. Currently, U-HRCT is considered to have the highest in-plane resolution of existing CT, but by combining U-HRCT and SR-DL, we were able to clearly depict the details of abnormal findings and normal anatomical structures of inflated fixed cadaveric human lungs and effectively reduce image noise compared to the original images of U-HRCT alone. In the visual evaluation, the super-resolution effect of SR-DL was observed clearly in GGO, bronchiectasis with bronchial wall thickening, emphysematous change, interlobular septal thickening, reticular opacity, and normal anatomical structures such as vessels, bronchi, and bronchioles. This margin sharpness was also shown in the objective evaluation by ERD and ERS using the CT attenuation profile. In GGO, the internal microstructure was visualized more conspicuously (Fig. 4).

While GGOs constructed with SR-DL displayed improved image quality, nodules and consolidations showed no significant difference in image quality between the c2048-image and the v2048-image (Fig. 5). It is known that the high-frequency region constitutes the edge of an image in the frequency domain of a digital image. Therefore, SR-DL constructs images of fine structures by estimating high-frequency components and adding them to the input image. However, nodules and consolidation are mostly composed of uniform and dense regions, and these characteristics are mainly defined by low-frequency

components in the frequency domain. Therefore, the effect of SR-DL might be poor on nodules and consolidation. Consequently, the v2048-image shows little difference from the c2048-image. To further investigate the difference of image quality improvement between nodules/consolidations and GGOs, the power spectrum of each images was obtained by performing fast Fourier transform (FFT). Figure 6 shows a GGO and consolidation in the same location in the c2048-image and v2048-image, respectively. The subtraction images of the FFT of the v2048-image minus the FFT of the c2048-image are also shown. In the GGO power spectrum, the FFT of the v2048-image (d) has a larger central white area than that of the c2048-image (b). In the subtraction image (e), the uniform gray area in the center is considered to be the common part, and the white-dominant donut-shaped area around the center is considered to be the part added by SR-DL. Furthermore, a black-dominant area in the periphery was considered to represent an element deleted by SR-DL. In the consolidation power spectrum, the donut-shaped region with white dominance in the subtraction image (j) is not as noticeable as in the case of the GGO. These results validate our hypothesis that GGOs are more strongly affected by SR-DL than nodules/consolidations. Therefore, SR-DL is expected to be a suitable super-resolution method in the depiction of fine structures.

The ultra-high-quality image constructed by SR-DL contains less image noise compared to conventional U-HRCT images. Many previous studies report that super-resolution and image noise reduction can be achieved simultaneously [10, 13–16]. While U-HRCT shows superior image quality, the U-HRCT image obtained from inflated fixed cadaveric human lungs does not show lung microstructures as expected from its high spatial resolution. On the other hand, the v2048-image shows unknown microstructures that have not been previously depicted by CT. It is speculated that the microstructures contained in raw data of U-HRCT are hidden under image noise, and conventional image reconstruction algorithms fail to reconstruct microstructure image data. Thus, to obtain CT images of lung microstructures with higher resolution, a new method of reconstructing high-resolution images from raw data of U-HRCT was warranted. Our results indicate that our SR-DL is suitable for this purpose. The reason that SR-DL can depict unknown microstructures could be due to its image noise reduction in addition to adding estimated high-frequency components. We conclude that our SR-DL is an algorithm that enables us to obtain CT images of lung microstructures with higher resolution.

This study has several limitations. First, the 2048-matrix image was evaluated by a single-blind test. However, there was a clear difference in image quality between the c2048-image and the v2048-image, and radiologists who evaluated the images could easily distinguish these images. Therefore, it was difficult to evaluate whether the blind test was well-established. Second, using c1024-images as a reference might not be appropriate, because there was no difference in image quality between c1024-image and c2048-image in the visual evaluation. This was because the FOV was set to 200 mm. Under this condition, each pixel size was about 0.2 mm in c1024-images and 0.1 mm in c2048-images. U-HRCT has a maximum spatial resolution of 0.14 mm in metal slit phantom experiments, but its actual spatial resolution in human tissue is expected to be more than 0.2 mm. Therefore, the pixel size had saturated the maximum spatial resolution in c1024-images, and the image quality did not improve in c2048-images.

In conclusion, the SR-DL developed in this study might be a promising tool for improving lung imaging quality to a level where it exceeds its original U-HRCT image and shows unknown microstructures that have not been previously depicted by CT. In the future, we will collect training and test datasets of living lungs and attempt to construct an optimal algorithm for clinical images.

Acknowledgements We would like to thank Mr. Noritoshi Ushio (Department of Radiology, Shiga University of Medical Science, Otsu, Shiga, Japan) for assisting us with the scans of the inflated fixed cadaveric human lungs. We would also like to thank Editage (www.editage.com) for English language editing.

Funding This work did not receive any specific grant from funding agencies in the public, commercial, or not-for-profit sectors.

Declarations

Conflict of interest Yoshiyuki Watanabe received a research grant from Canon Medical Systems Corp. All other authors declare that they have no conflict of interest.

Ethical approval This work was approved by the local institutional review board (No. R2020-178).

References

1. Higaki T, Nakamura Y, Tatsugami F, Nakaura T, Awai K. Improvement of image quality at CT and MRI using deep learning. Jpn J Radiol. 2019;37:73–80.
2. Dong C, Loy CC, He K, Tang X. Image super-resolution using deep convolutional networks. IEEE Trans Pattern Anal Mach Intell. 2016;38:295–307.
3. Umehara K, Ota J, Ishida T. Application of super-resolution convolutional neural network for enhancing image resolution in chest CT. J Digit Imaging. 2018;31:441–50.
4. Hata A, Yanagawa M, Honda O, Kikuchi N, Miyata T, Tsukagoshi S, et al. Effect of matrix size on the image quality of ultra-high-resolution ct of the lung: comparison of 512 × 512, 1024 × 1024, and 2048 × 2048. Acad Radiol. 2018;25:869–76.

5. Yanagawa M, Hata A, Honda O, Kikuchi N, Miyata T, Uranishi A, et al. Subjective and objective comparisons of image quality between ultra-high-resolution CT and conventional area detector CT in phantoms and cadaveric human lungs. Eur Radiol. 2018;28:5060–8.
6. Iwasawa T, Sato M, Yamaya T, Sato Y, Uchida Y, Kitamura H, et al. Ultra-high-resolution computed tomography can demonstrate alveolar collapse in novel coronavirus (COVID-19) pneumonia. Jpn J Radiol. 2020;38:394–8.
7. Markarian B, Dailey ET. Preparation of inflated lung specimens. In: Groskin SA, editor. The lung: radiologic-pathologic correlations. 3rd ed. St. Louis: Mosby; 1993. p. 4–12.
8. Kim J, Lee J, Lee KM. Accurate image super-resolution using very deep convolutional networks. IEEE Conf Comp Vision Pattern Recogn (CVPR). 2016;2016:1646–54.
9. Boehm T, Willmann JK, Hilfiker PR, Weishaupt D, Seifert B, Crook DW, et al. Thin-section CT of the lung: does electrocardiographic triggering influence diagnosis? Radiology. 2003;229:483–91.
10. Tatsugami F, Higaki T, Nakamura Y, Yu Z, Zhou J, Lu Y, et al. Deep learning-based image restoration algorithm for coronary CT angiography. Eur Radiol. 2019;29:5322–9.
11. Kanda Y. Investigation of the freely available easy-to-use software "EZR" for medical statistics. Bone Marrow Transplant. 2013;48:452–8.
12. Hansell DM, Bankier AA, MacMahon H, McLoud TC, Müller NL, Remy J. Fleischner society: glossary of terms for thoracic imaging. Radiology. 2008;246:697–722.
13. Park J, Hwang D, Kim KY, Kang SK, Kim YK, Lee JS. Computed tomography super-resolution using deep convolutional neural network. Phys Med Biol. 2018. https://doi.org/10.1088/1361-6560/aacdd4.
14. Kang E, Min J, Ye JC. A deep convolutional neural network using directional wavelets for low-dose X-ray CT reconstruction. Med Phys. 2017;44:e360–75.
15. Du W, Chen H, Wu Z, Sun H, Liao P, Zhang Y. Stacked competitive networks for noise reduction in low-dose CT. PLoS ONE. 2017. https://doi.org/10.1371/journal.pone.0190069.
16. Akagi M, Nakamura Y, Higaki T, Narita K, Honda Y, Zhou J, et al. Deep learning reconstruction improves image quality of abdominal ultra-high-resolution CT. Eur Radiol. 2019;29:6163–71.